

Resolution study of laser-ultrasound technique for disbonds detection in multilayered metallic structures

Patrycja PYZIK D, Łukasz AMBROZIŃSKI

AGH University of Krakow, Al. Mickiewicza 30, 30-059 Kraków

Corresponding author: Patrycja PYZIK, email: pyzikp@agh.edu.pl

Abstract: Multilayered metallic structures, such as adhesively bonded aluminum plates, are increasingly used as construction elements for their reduced weight and strong mechanical properties. However, nondestructive inspection of these components is challenging due to multiple reflections and mode conversions in traditional ultrasonic scans. Laser ultrasound (LU), a fully optical, non-contact technique, offers fast and efficient inspection with high-resolution performance. LU generates a broad range of frequencies, and shear modes can be efficiently produced in the thermoelastic regime using low laser energies. This paper analyses the resolution of a laser-generated shear wave technique for inspecting adhesively bonded aluminum plates. Multiphysics finite-difference simulations are performed on a two-layer aluminum plate model bonded with an epoxy film, incorporating a defect simulating delamination. Various defect depths are examined to evaluate the technique's resolution, and the simulation results are validated through experiments on a structure composed of three aluminum plates bonded with an epoxy film.

Keywords: laser ultrasound, shear waves, finite difference simulation, resolution study.

1. Introduction

Adhesively bonded metals are increasingly used in many modern industries including automotive and aerospace. These are high-strength structures with reduced weight. The increased strength is obtained due to adhesive bonding which provides stress distribution over the entire bonding area [1]. Despite numerous advantages, this type of bond is often affected by many particular defects such as disbonds, delaminations and porosity.

One of the methods used for adhesive layer testing is X-Ray radiography. Although this technique can detect voids and porosity in the adhesive layer [2], it is insensitive to non-volumetric defects, such as disbonds and delaminations. It also requires double-side access to material under test. Conventional ultrasounds is an alternative [1, 2] which however requires the use of coupling agents and thus cannot be classified as non-contact technique.

This limitation can be addressed using electromagnetic acoustic transducers (EMATs), a commonly used method for non-destructive testing of metallic structures. EMATs have been successfully applied to generate shear waves in metals [3], as well as for weld inspection using shear horizontal waves [4]. Nevertheless, EMAT probes are typically designed to operate with minimal lift-off, usually remaining within 1 mm of the surface. Moreover, their effectiveness in producing high-resolution B-mode images is limited. This is primarily due to two factors: their narrow bandwidth and their relatively large size, both of which constrain the precision and clarity of the resulting images [4].

In contrast, laser ultrasound (LU) can generate ultra-wideband ultrasound signals, not achievable with any other techniques, in totally non-contact and all-optical approach [1, 5]. Its undeniable advantage over EMATs is the ability to perform inspections from considerably larger distances. LU has shown great potential in high-resolution imaging of carbon-reinforced composites [6-8] using longitudinal waves. For metallic structures, however, the excitation of elastic waves in the normal direction is inefficient [9, 10] In recent years, the zero-group velocity Lamb modes were proposed as an alternative to classical bulk waves for nondestructive testing of plate structures [11].

Our approach presented in [12] involves using laser-generated shear waves to inspect adhesive bonds in metallic structures. The generated waves propagate at an oblique angle in the structure under test and are scattered at each discontinuity appearing along their path. Therefore, the optimal source-detector distance was found to maximize the amplitude of shear waves reflected from a given depth and detected at the sample surface.

In this paper, we investigate the resolution of the method presented in [12] with the experiment performed on a sample consisting of three epoxy-bonded aluminum plates, with an artificial defect created with a Teflon insert in the first adhesive layer. The results are supported with multiphysics Finite Difference (FD) and Local Interaction Simulation Approach (LISA) simulations .

2. Materials and methods

2.1. Laser ultrasound excitation

The physical mechanism of ultrasounds excitation by laser source depends on the excitation power [13]. Although the amplitudes of the propagating waves are significantly lower for the thermo-elastic region than due to material ablation, the non-destructive testing requirement imposes the operation below 10^7 W/cm² power density limit.

For an isotropic material, the excitation mechanism in the thermo-elastic regime (neglecting the heat produced by mechanical deformation, and the second derivative of the temperature T) is described by the following set of coupled differential equations:

$$k\nabla^2 T = \rho c_V \dot{T} - q,\tag{1}$$

$$\mu \nabla^2 \mathbf{u} + (\lambda + \mu) \nabla (\nabla \cdot \mathbf{u}) = \rho \ddot{\mathbf{u}} + \beta \nabla T, \tag{2}$$

where k is the thermal conductivity coefficient, T is the temperature in the material, ρ is the material density, c_V is the specific heat at constant volume, q is the power density of the heat source created by laser irradiation, \boldsymbol{u} is the unknown displacement vector due to the thermoelastic effect, λ and μ are the Lame constants, and β is the thermo-acoustic coupling constant related to the linear thermal expansion coefficient α_T as $\beta=(3\lambda+2\mu)\alpha_T$.

Equation (1) describes thermal conductivity and thermal expansion due to the change of temperature T, and (2) is a description of propagating elastic wave excited by the thermal expansion $\beta \nabla T$. To obtain the elastic displacements due to thermal source, this set of the coupled equations was solved using numerical procedures.

2.2. Numerical models

Figure 1 presents diagrams of the damage imaging problem. The inspection is performed exciting ultrasonic waves by laser pulse absorbed at the upper surface of the sample. To assess damage imaging both the source and detectors set at a given spacing are scanned over the surface.

Numerical modeling of the wave generation process requires multiphysics approach that accounts for coupling of the heat transfer and the elastic wave equations. In this part of research, the elastic displacements generated by a laser heat source are obtained from a two-dimensional (2D) coupled thermoelasticity model developed using Finite Difference approach and its extension – LISA [14, 15]. LISA is introduced for solving the linear elastic wave equation, while FD scheme is applied to evaluate the temperature distributions due to a thermal source.

Two 2-dimensional (2D) multilayered models were created. The material properties for both models were defined as density $\rho = 2700 \text{ kg/m}^3$, Young's modulus E = 68.9 GPa, Poisson's ratio $\nu = 0.33$ for aluminum plates and $\rho = 1540 \text{ kg/m}^3$, E = 3.5 GPa, $\nu = 0.33$ for epoxy bonding.

The first model (Model 1), presented in Figure 1a was used to investigate the lateral resolution of shear-waves based inspection approach. In contrast to elevation resolution, which remains constant regardless of depth and is primarily determined by the excitation beam width, lateral resolution appears to vary with the depth of the defect. This is due to the decreasing amplitude of reflected waves as the defect is located deeper below the surface. To account for different defect depths, the model was designed with two aluminum layers, with the top layer thickness ranging from 1 mm to 5 mm.

The defect in the form of a 4 mm long air gap was placed at the epoxy film. For each case, the total thickness of the model and the thickness of epoxy layer was equal to 6 mm and $4.2~\mu m$ respectively. To reduce the influence of waves reflections from the edges, the length of the model varied from 20 to 32 mm for different scenarios.

In order to compare simulation results with the experiment, a model (Model 2) resembling the tested sample was created (Figure 1b). The 20 mm long model consisted of three aluminum layers with thicknesses 1 mm, 1.25 mm, and 3.5 mm, bonded with epoxy film. The defect as an air gap was introduced at the first interface.

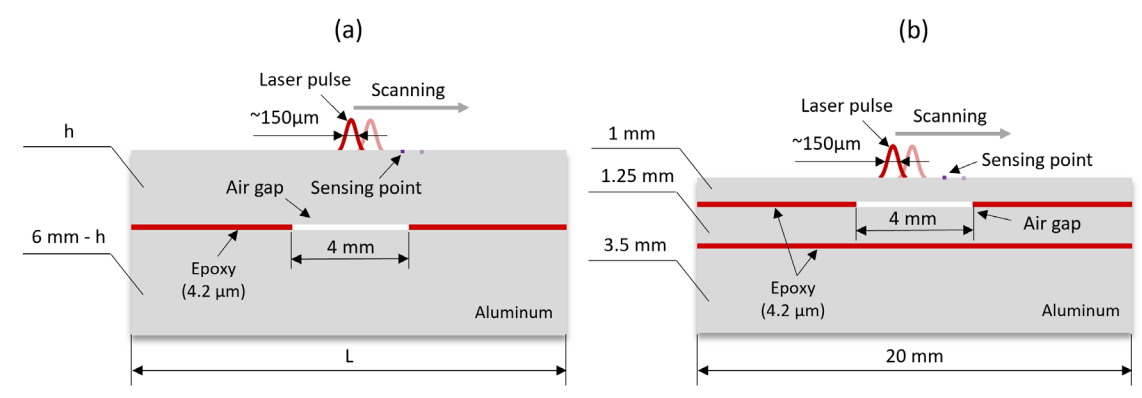


Figure 1. Schematics of the simulated models. (a) Model 1 consisting of two aluminum plates of varying thicknesses, bonded with an epoxy layer. (b) Model 2 resembling the sample tested in the experiment. The model consisted of three bonded aluminum plates of – 1, 1.25, and 3.5 mm thicknesses. For each case, the defect was modeled as an 4 mm – long air gap at the first epoxy layer.

Both models were excited with Super-Gaussian pulse of width 150 μ m, duration 15 ns and energy 1 mJ resulting in peak power $Q_0 \cong 65.33$ kW and peak power density of 7.84 GW/m². After recalculations, the value of power density is equal to 7.84 \cdot 10⁵ W/cm², which satisfies the 10⁷ W/cm² limit for thermoelastic generation provided in Sect.2.1. Spatial - f(x) and temporal - g(t) characteristics of laser pulse normalized to the maximum amplitude equal to Q_0 are presented in Figure 2 (a) and (b) respectively. The width of the pulse and the time duration are defined as full width at half maximum (FWHM) of given characteristic [16]. Panel (c) of Figure 2 illustrates the spatio-temporal map of power Q distributed along the X-axis on the sample's surface, which was obtained as $Q_0 \times f(x) \times g(t)$.

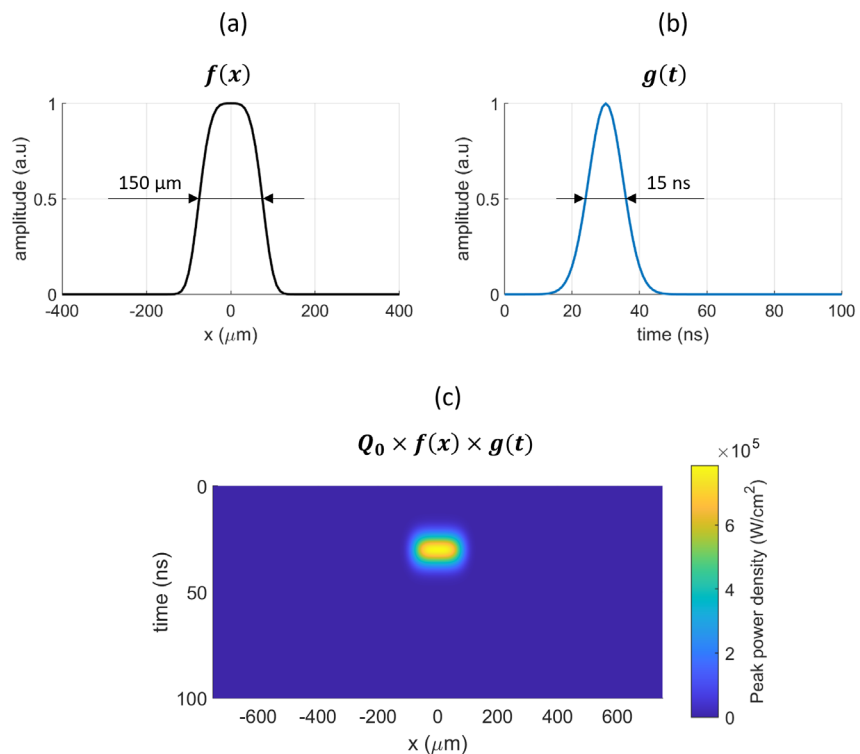


Figure 2. (a) Spatial characteristic of Super-Gaussian laser pulse of the width equal to 150 μm indicated as full width at half maximum (FWHM). (b) Temporal characteristic of laser beam of duration equal to 15 ns defined as the FWHM of the Gaussian pulse. (c) The spatio-temporal map of power *Q* distributed along the *x*-axis on the sample's surface.

The simulation parameters – time and space discretization – were chosen as dt=1 ns and $dx \cong 8.33$ µm, to ensure the Courant-Friedrich-Lewy (CFL) stability condition. The model was uniformly sampled at both directions, thus dy was equal to dx. For both models, a laser pulse was applied at the top

surface and a set of simulations for multiple positions of the excitation-detector pair along the horizontal axis was performed. The source-receiver distance was adjusted for each scenario to maximize the amplitude of reflected shear wave, according to the optimization provided in [12]. Out-of-plane velocity signals were collected to obtain B-scan images presented in Sect. 3.1.

2.3. Experimental setup

Experiments were performed using a non-contact system (Figure 3) consisting of a diode-pumped laser for excitation and a fiber-optic Sagnac interferometer for detection [17, 18]. The involvement of optical devices allowed for all-optical measurements, thus, the acquisition was performed without any contact with the specimen under test. Pulses from a diode-pumped nanosecond laser were firstly reflected from the mirror, as presented in panel (a) of Figure 3 and then focused using the lens to form a thin excitation line on the sample surface. The laser pulse energy was approximately 1 mJ to remain in thermoelastic regime and ensure the integrity of the material.

A plate consisting of three aluminum layers – 1, 1.25, and 3.5 mm-thick, bonded using epoxy film, was inspected. The damage was introduced to the structure by placing a 15×15 mm Teflon insert at the first interface during the manufacturing process.

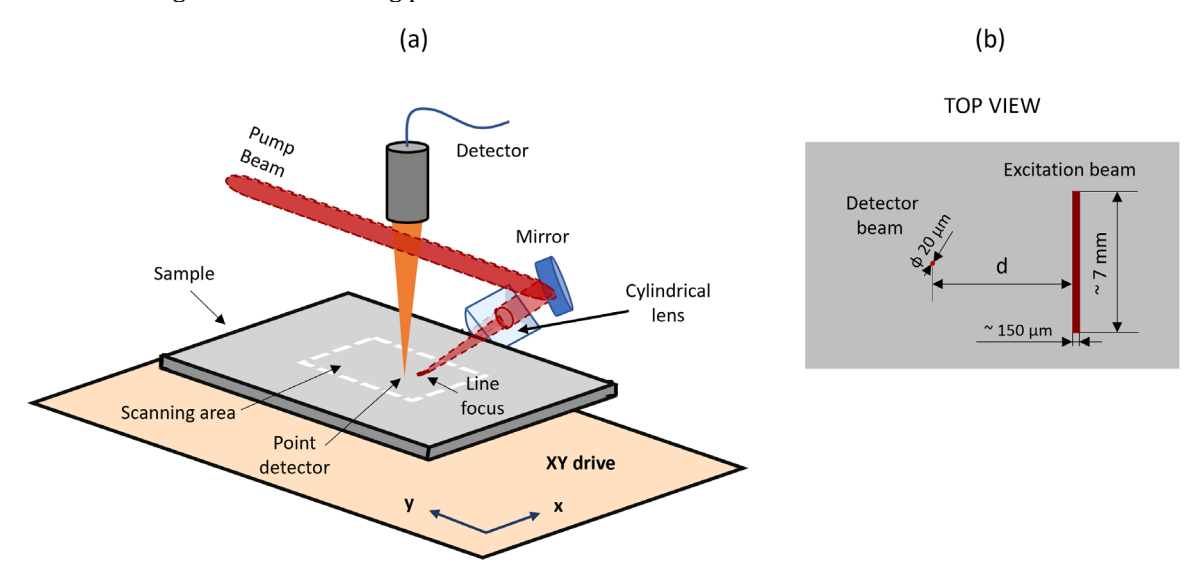


Figure 3. (a) Schematic of laser ultrasound inspection system. (b) Top view for laser beams alignment.

Figure 3(b) illustrates the top view for laser beams alignment. The laser source was about 150 μm width and 7 mm length and the detector spot was 20 μm in diameter. To maximize the amplitude of defect-reflected shear waves, the source-receiver distance d was set to 2 mm, according to the analysis provided in [12]. The source-receiver pair remained unmoved during the measurement, since their stability is crucial for data interpretation. Hence, the scanning was performed by the translation stage supporting the sample, which enabled the movement in XY-plane.

The area of 25×25 mm was scanned with the scanning resolution of 0.02 mm, resulting in 1250×1250 mesh of points. For each point, the time signals (A-scans) were acquired. A series of A-scans collected along a line is compiled to form a B-scan. The B-scan image, presented in Figure 4a, was initially pre-processed using spatial filtration. Although slight differences between the time signals in the damaged and undamaged regions can be observed in panel (b) of Figure 4, the strong dominance of surface waves combined with a low signal-to-noise ratio (SNR) hinders accurate damage detection.

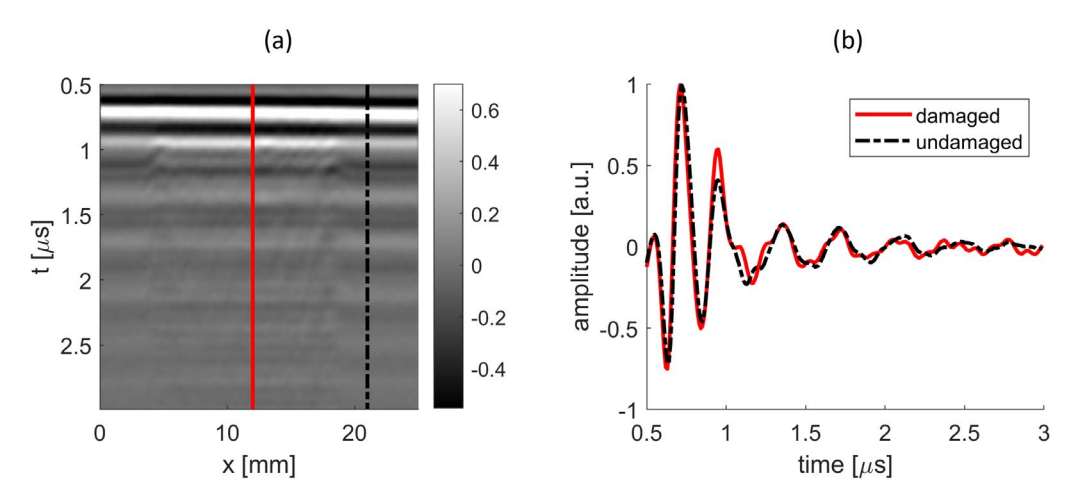


Figure 4. (a) A pre-processed B-scan obtained from scanning along x axis. (b) Exemplary time signals acquired at x = 12 mm, from damaged (red) and at x = 21 mm, from undamaged (dashed black) area.

3. Results

3.1. Resolution study

The signals collected from the simulation of pristine Model 1 were subtracted from the damage ones. The separated shear waves can be observed in resulting B-scan (Figure 5a). To obtain the edge profile (Figure 5b) a cross-section of the B-scan at time-of-flight (TOF) corresponding to the maximum amplitude of the shear wave reflection was performed. Then a sigmoid function \mathcal{C} given as:

$$C(x) = a \cdot \left(1 - \frac{1}{1 + \exp(-b \cdot (x - c))}\right)$$
(3)

was fitted to the amplitude profile and the resolution was obtained using the full width at half amplitude of the derived function C [19]. The estimation was carried out for each simulated defect location, ranging from 1 mm to 5 mm in 0.5 mm increments. For clarity, only five of the nine resulting images are shown in Figure 6 (a)-(e). The obtained depth-resolution dependence is illustrated in Figure 6f. It is observed that the method's resolution decays with depth. The trend remains approximately linear across most of the range. However, at the 4 mm defect depth, a distinct artifact appears in the simulated B-

scan. This anomaly could result from multiple reflections involving the mode-converted S-L wave [12].

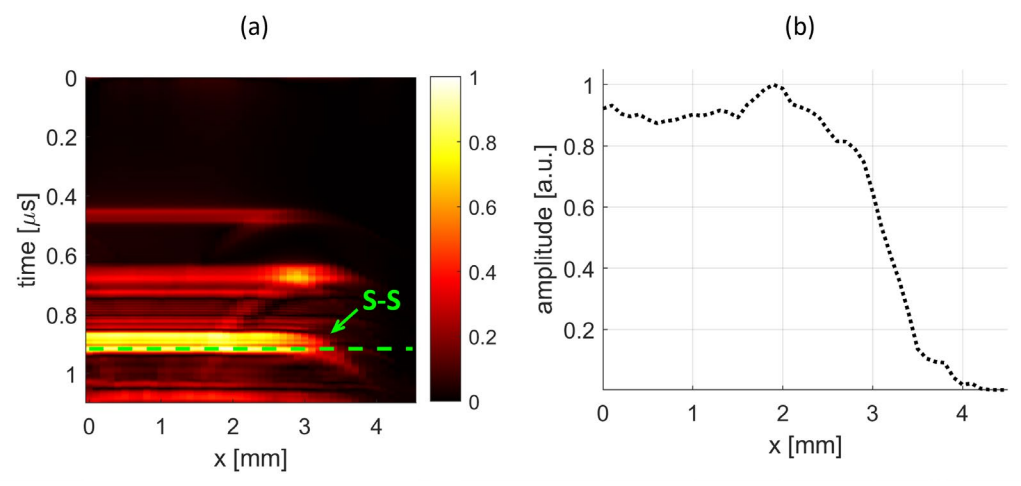


Figure 5. (a) B-scan obtained as the envelope of the difference between out-of-plane signals for pristine and damage cases, for air gap location depth equal to 1mm. A green dashed line indicates the maximum amplitude of the reflected shear wave. Reproduced from [12]. (b) One-dimensional edge profile obtained as the cross-section of the B-scan from panel (a) at time corresponding to the maximum amplitude of the shear wave reflection.

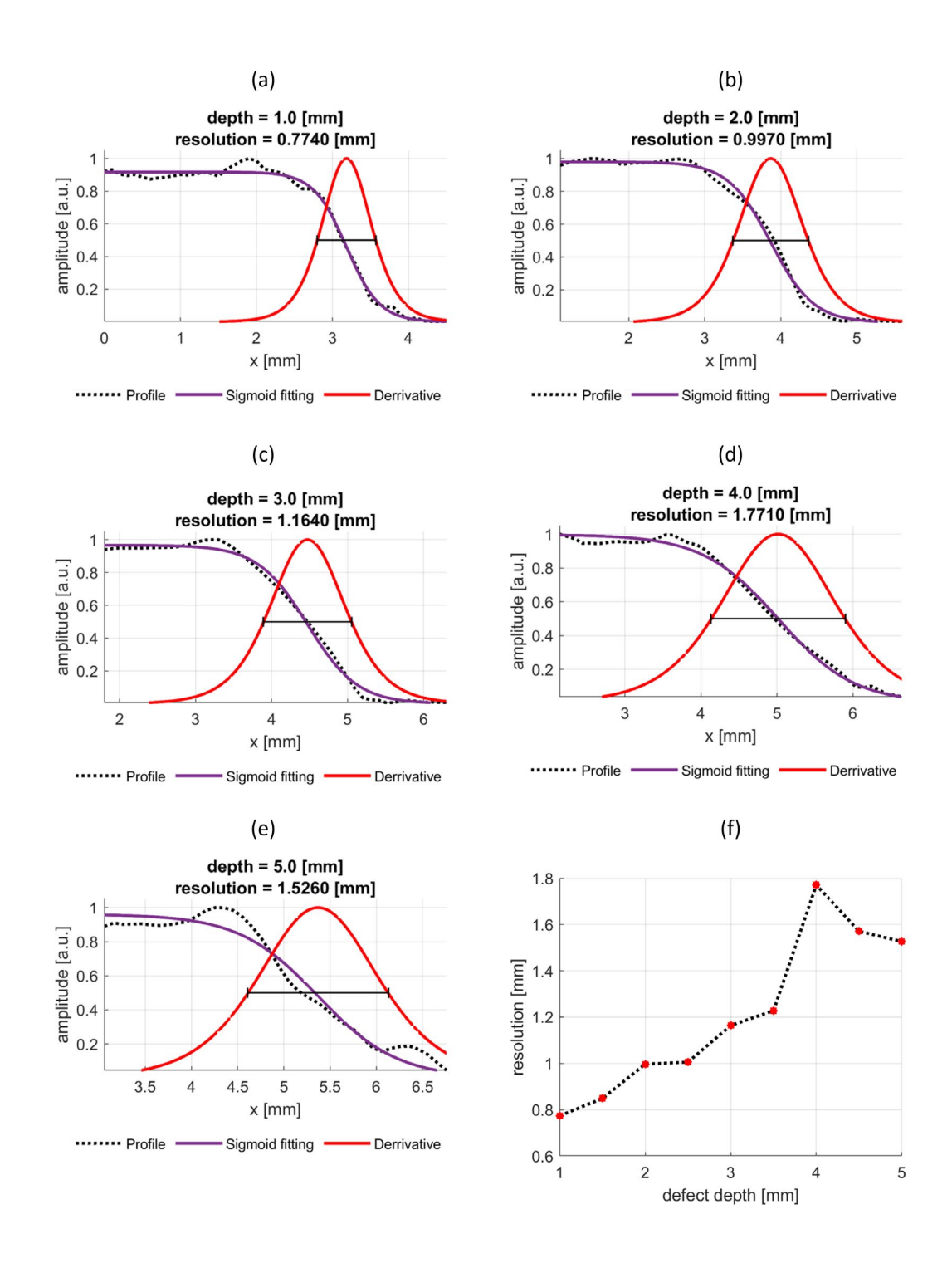


Figure 6. Panels (a) – (e): One-dimensional edge profiles obtained as the cross-section of the B-scans at time corresponding to the maximum amplitude of the shear wave reflection with sigmoid fitting and its derivative for models with defect depth ranging from 1 mm to 5mm.

Panel (f): Resolution as a function of defect depth – reproduced from [12].

3.2. Experimental evaluation

For experimental evaluation of resolution study presented above, the simulation and experimental data were compared. The data collected from bonded aluminum sample was used — the experiment and specimen parameters are detailed in Sect. 2.3.

In order to prepare the image comparable to the simulation one, the subtraction was performed. The reference B-scan, shown in Figure 7a, was obtained through the averaging of measurements from the undamaged area. Then the pristine image was subtracted from the pre-processed acquired data, presented previously in Figure 4a. The resulting B-scan revealing damage-reflected wave modes is illustrated in Figure 7b.

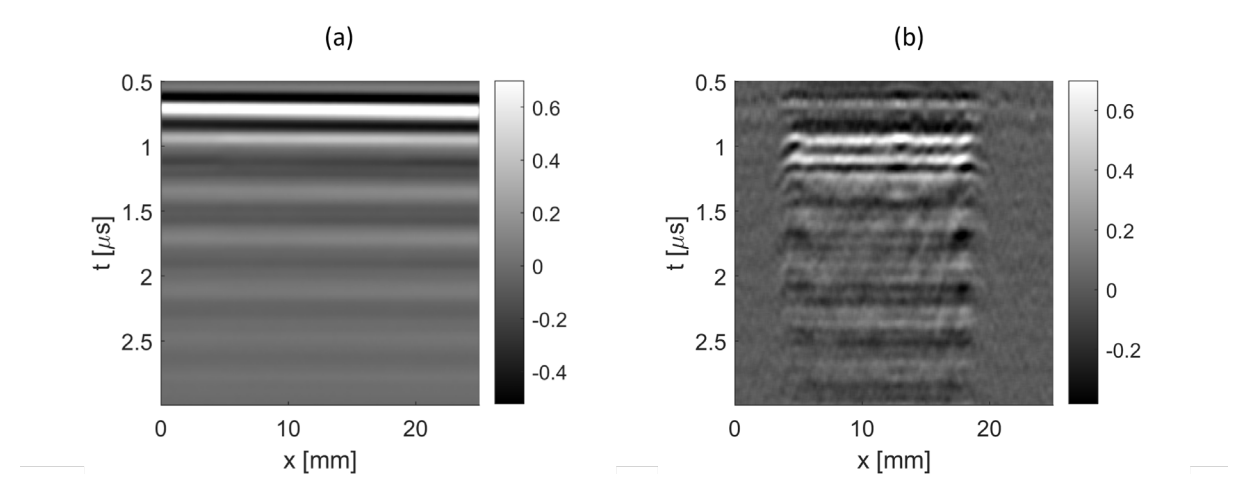


Figure 7. (a) Reference B-scan averaged over undamaged part of the specimen. (b) B-scan obtained after subtraction of reference in panel (a) from pre-processed image presented in Figure 4a.

The full dataset collected from scanning the 25×25 mm area of the specimen was processed using reference subtraction. This approach enabled the generation of C-scan images showing the defect located 1 mm beneath the surface, as illustrated in Figure 8. Panel (a) presents a C-scan based on signal amplitudes at a TOF of 0.95 μ s, corresponding to the shear wave (S-S) reflection from the first bonding layer. In contrast, panel (b) uses an arbitrarily chosen TOF of 1.25 μ s. As expected, optimizing the time-of-flight to match the peak amplitude of the S-S wave results in improved image quality and enhanced signal-to-noise ratio.

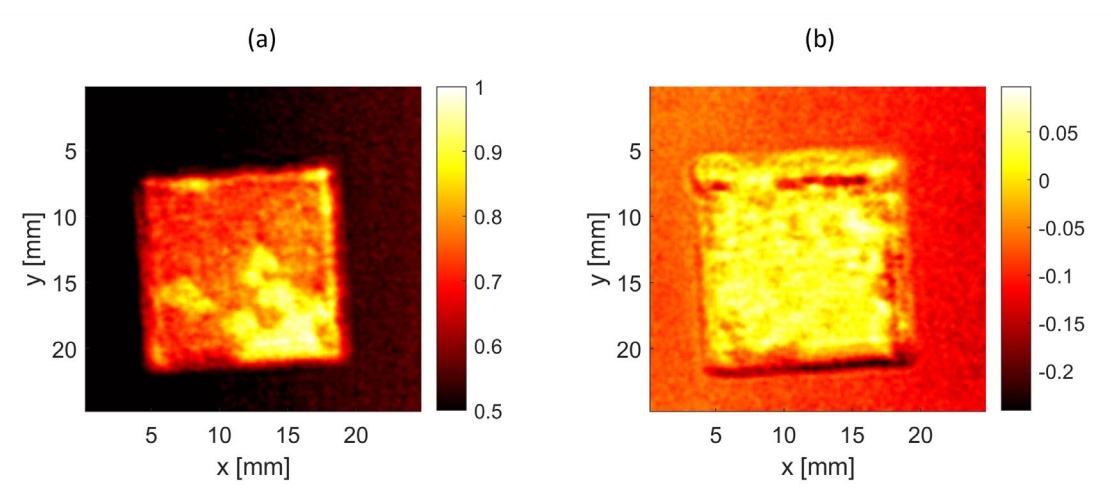


Figure 8. C-scan in tested sample using 3D data for (a) $TOF = 0.95 \mu s$ corresponding to the S-S wave arrive from the defective region and (b) arbitrarily selected $TOF = 1.25 \mu s$, presenting lower SNR.

The simulation data was obtained with Model 2, detailed in Sect. 2.2. A set of simulations resembling experimental scanning were performed and the collected data resulted in a B-scan. The signals were initially lowpass-filtered with a cut-off frequency of 9 MHz. The filtration allowed to suppress the wave modes that could not be observed in experimental data due to the limitations of measurement equipment. Otherwise, the high-frequency components could affect the results so that the simulation and experimental data were

not comparable. Then, the pristine model (without a defect induced) was simulated using the same configuration and the results were low-pass filtered. Analogously, the difference between signals from a pristine model and the damage ones was calculated.

The B-scans, generated as the envelope of the difference between out-of-plane signals from the damaged and reference cases, are shown in Figure 9 (a) and (c). These scans reveal the shear wave reflected from the defect, indicated by a green dashed line. The corresponding edge profiles—taken as cross-sections along the time line of maximum amplitude—are presented in panels (b) and (b) for the simulation and the experiment, respectively.

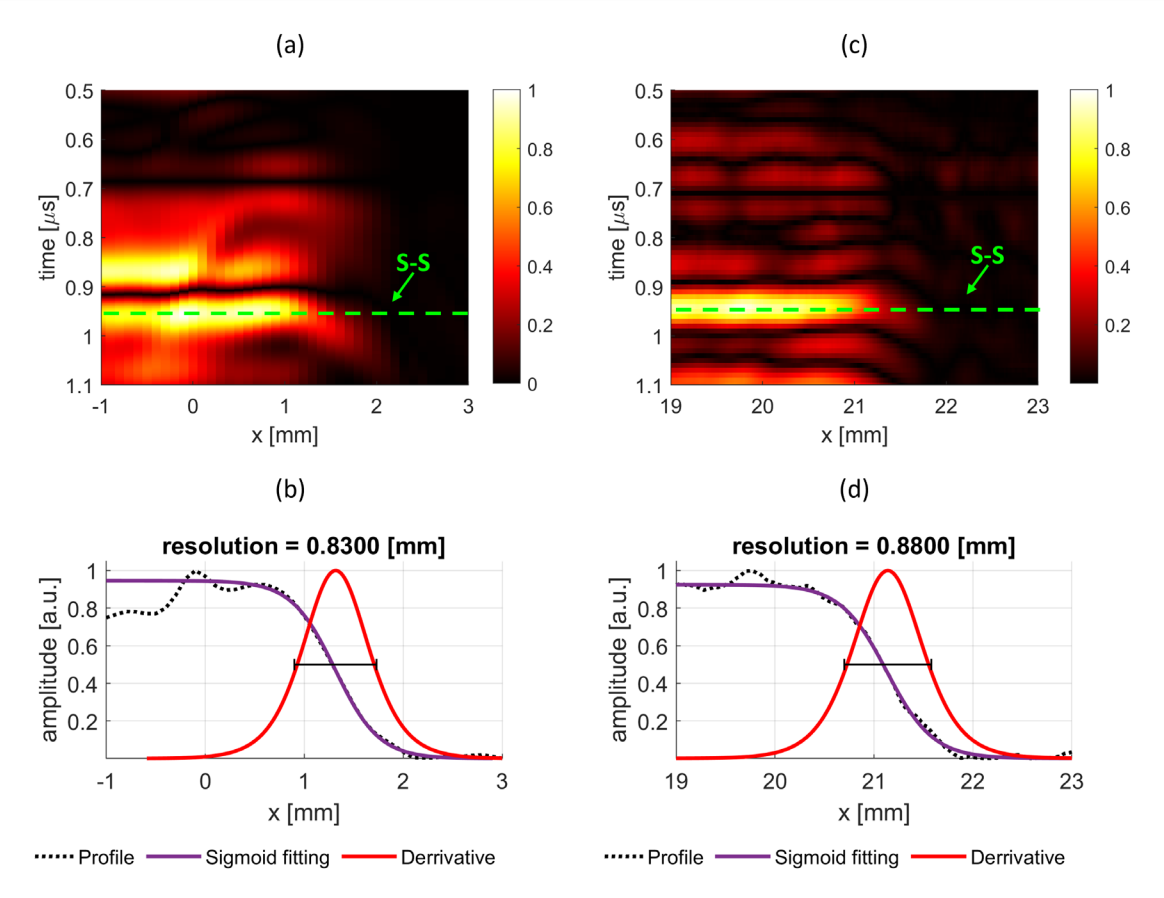


Figure 9. B-scans obtained as the envelope of the difference between out-of-plane reference signals and damaged ones for data collected from simulation of Model 2 (a), and experimental data (c). Green dashed lines indicate the maximum amplitude of the reflected shear wave. Panels (b) and (d) presents edge profiles obtained as the cross-section of the B-scans at time corresponding to the maximum amplitude with sigmoid fitting for simulation and experiment cases respectively.

The resolution estimated using the procedure proposed in this paper equals $0.83~\mathrm{mm}$ for the simulation and $0.88~\mathrm{mm}$ for the experiment. The minimal mismatch between values indicates that the presented method for resolution evaluation using simulation data is reliable. The value of resolution for the defect depth equal to $1~\mathrm{mm}$ was estimated in method's resolution study in Sect. $3.1~\mathrm{as}~0.77~\mathrm{mm}$. The inconsistency of values obtained for simulations — $0.77~\mathrm{mm}$ and $0.83~\mathrm{mm}$ — could be caused by the difference in models. The waves modes reflected from the second epoxy layer in Model 2 probably disturb the results. It indicates that the method's resolution study gives only the rough view on how the resolution changes with depth. In order to obtain more accurate values, the resolution study should be performed for each individual case.

4. Conclusions

As presented in our previous studies the inspection of multilayered aluminum structures can be effectively performed using an all-optical laser ultrasound system. Since longitudinal waves are not efficiently generated in metals under thermo-elastic excitation, shear waves can be effectively utilized. Since these wave are excited at an oblique angle, careful analyses are needed to optimize the setup, develop post processing algorithms as well as interpret the final results.

In this paper, a dedicated resolution study of LU-based bonded-metallic inspection was presented. Numerical modeling played a key role in the evaluation of the method's resolution. Finite-Difference (FD) simulations, along with the Local Interaction Simulation Approach (LISA), were essential for predicting wave propagation and estimating resolution limits.

The analysis, supported by both simulations and experiments, revealed that lateral resolution decreases almost linearly with increasing defect depth. The consistency between simulated and experimental resolution values confirms the accuracy and applicability of the proposed approach. The work presented in this paper considered 2D problem in the plane at which the source-receivers were located. Additional study is required, however, to evaluate the third dimension and provide the comprehensive data on the entire imaging system.

Additional information

The author(s) declare: no competing financial interests and that all material taken from other sources (including their own published works) is clearly cited and that appropriate permits are obtained.

References

- 1. C. C. Guyott, P. Cawley, R. D. Adams; The Non-destructive Testing of Adhesively Bonded Structure: A Review; J. Adhes, 1986, 20(2), 129-159; DOI: 10.1080/00218468608074943
- 2. R. D. Adams and B. W. Drinkwater; Nondestructive testing of adhesively-bonded joints; NDT and E International, 1997, 30(2), 93-98; DOI: 10.1016/S0963-8695(96)00050-3
- 3. J. Parra-Raad, P. Khalili, F. Cegla; Shear waves with orthogonal polarisations for thickness measurement and crack detection using EMATs; NDT and E International, 2020, 111, 102212; DOI: 10.1016/j.ndteint.2019.102212
- 4. H. J. Salzburger, G. Dobmann, H. Mohrbacher; Quality control of laser welds of tailored blanks using guided waves and EMATs; IEE Proceedings: Science, Measurement and Technology, 2001, 148, 143–148; DOI: 10.1049/ip-smt:20010534
- 5. C. B. Scruby, L. E. Drain; Laser Ultrasonics: Techniques and Aplications; Taylor & Francis Group, 1990; DOI: 10.1201/9780203749098
- 6. L. Ambrozinski, J. Mrowka, M. O'Donnell, I. Pelivanov; Detection and imaging of local ply angle in carbon fiber reinforced plastics using laser ultrasound and tilt filter processing; Compos Part A Appl Sci Manuf, 2019, 126, 1005581; DOI: 10.1016/j.compositesa.2019.105581
- 7. I. Pelivanov et al.; High resolution imaging of impacted CFRP composites with a fiber-optic laser-ultrasound scanner; Photoacoustics, 2016, 4(2), 55–64; DOI: 10.1016/j.pacs.2016.05.002
- 8. I. Pelivanov, Ł. Ambrozinski, M. O'Donnell; Heat damage evaluation in carbon fiber-reinforced composites with a kHz A-scan rate fiber-optic pump-probe laser-ultrasound system; Compos Part A Appl Sci Manuf, 2016, 84, 417–427; DOI: 10.1016/j.compositesa.2016.02.022
- 9. A. M. Aindow, R. J. Dewhurst, D. A. Hutchins, S. B. Palmer; Laser-generated ultrasonic pulses at free metal surfaces; J Acoust Soc Am, 1981, 69(2), 449–455; DOI: 10.1121/1.385470
- 10. D. A. Hutchins; 2-Ultrasonic Generation by Pulsed Lasers; Physical Acoustics, 1988, 18, 21-123; DOI: 10.1016/B978-0-12-477918-1.50008-4
- 11. J. Spytek, A. Ziaja-Sujdak, K. Dziedziech, L. Pieczonka, I. Pelivanov, L. Ambrozinski; Evaluation of disbonds at various interfaces of adhesively bonded aluminum plates using all-optical excitation and detection of zero-group velocity Lamb waves; NDT and E International, 2020, 112, 102249; DOI: 10.1016/j.ndteint.2020.102249
- 12. P. Pyzik, A. Ziaja-Sujdak, J. Spytek, M. O'Donnell, I. Pelivanov, L. Ambrozinski; Detection of disbonds in adhesively bonded aluminum plates using laser-generated shear acoustic waves; Photoacoustics, 2021, 21,100226, 2021; DOI: 10.1016/j.pacs.2020.100226
- 13. I. Arias, J. D. Achenbach; Thermoelastic generation of ultrasound by line-focused laser irradiation; Int J Solids Struct; 2003, 40(25), 6917–6935; DOI: 10.1016/S0020-7683(03)00345-7
- 14. P. P. Delsanto, R. S. Schechter, H. H. Chaskelis, R. B. Mignogna, R. Kline; Connection machine simulation of ultrasonic wave propagation in materials . II : The two-dimensional case; Wave Motion, 1994, 20, 295–314
- 15. P. Packo et al.; Numerical simulations of elastic wave propagation using graphical processing units-Comparative study of high-performance computing capabilities; Comput Methods Appl Mech Eng, 2015, 290, 98–126; DOI: 10.1016/j.cma.2015.03.002
- 16. G. Thériault; The beginner's guide on spot size of laser beam;

- https://www.gentec-eo.com/blog/spot-size-of-laserbeam#:~:text=FWHM%20(Full%20width%20at%20half,its%20point%20of%20maximum%20in tensity (accessed: May 24, 2024)
- 17. I. Pelivanov, T. Buma, J. Xia, C. W. Wei, M. O'Donnell; A new fiber-optic non-contact compact laser-ultrasound scanner for fast non-destructive testing and evaluation of aircraft composites; J Appl Phys, 2014, 115(11),1–11; DOI: 10.1063/1.4868463
- 18. I. Pelivanov, A. Shtokolov, C. W. Wei, M. O'Donnell; A 1 kHz a-scan rate pump-probe laser-ultrasound system for robust inspection of composites; IEEE Trans Ultrason Ferroelectr Freq Control, 2015, 62(9), 1696–1703; DOI: 10.1109/TUFFC.2015.007110
- 19. M. A. Kirby et al.; Spatial resolution in dynamic optical coherence elastography; J Biomed Opt, 2019, 24(09), 1-16; DOI: 10.1117/1.jbo.24.9.096006
- © **2025 by the Authors.** Licensee Poznan University of Technology (Poznan, Poland). This article is an open access article distributed under the terms and conditions of the Creative Commons Attribution (CC BY) license (http://creativecommons.org/licenses/by/4.0/).